

11. März 1993

# JOURNAL DE

# PHYSIQUE



Volume 3  
N° 1  
January 1993

II

Sektion  
Universität  
Bibliothek der TH  
S Eichstrasse 2 • 7000 Stuttgart 2

The European Physical Society

Jointly published by  
the Société Francaise de Physique  
and the Comité National de la Physique



sique

## CONTENTS

Editorial .....	D. JÉRÔME	V
<b><i>Short Communications</i></b>		
Surface diffraction studies of 2D crystals of short fatty alcohols at the air-water interface. ..... A. RENAULT, J.F. LEGRAND, M. GOLDMANN and B. BERGE	761	
Ultrasound scattering by buoyancy driven flows. ..... J.F. PINTON, C. LAROCHE, S. FAUVE and C. BAUDET	767	
<b><i>Atomic, Molecular and Cluster Physics</i></b>		
Investigation of the penning ionization mechanism of H <sub>2</sub> O by He* (2 <sup>1</sup> S, 2 <sup>3</sup> S) and Ne* (3P <sub>0</sub> , 3P <sub>2</sub> ). ( <i>Text in French</i> ). .... André LE NADAN, Guillaume SINOU and Firmin TUFFIN	775	
<b><i>Chemical Physics</i></b>		
Molecular theory of order electricity. .... M.A. OSIPOV and T.J. SLUCKIN	793	
Symmetry, structural phase transitions and phase diagram of Langmuir monolayers. .... V.M. KAGANER and V.L. INDENBOM	813	
Dynamics of spontaneous emulsification. .... R. GRANEK, R.C. BALL and M.E. CATES	829	
Columnar phases of pyramidal amphiphiles spread at the air-water interface. ..... A. EL ABED, P. MULLER, P. PERETTI, F. GALLET and J. BILLARD	851	
Pattern formation in the splay Fredericks transition of a nematic side-group polysiloxane. ..... Norbert SCHWENK and Hans Wolfgang SPIESS	865	
Confinement of dilute solutions of living polymers. ..... V. SCHMITT, F. LEQUEUX and C.M. MARQUES	891	
Spiral textures in lyotropic liquid crystals: first order transition between normal hexagonal and lamellar gel phases. .... K.M. MCGRATH, P. KÉKICHEFF and M. KLÉMAN	903	
Direct osmotic pressure measurements on partially neutralized poly(acrylic acid) gels. ..... C. WEILL, T. LACHHAB and P. MOUCHERONT	927	
Dependence of viscoelastic properties on spacer length and molecular weight for a side-chain liquid crystal polymer in a nematic solvent. .... D. GU, S.R. SMITH, A.M. JAMIESON, M. LEE and V. PERCEC	937	
<b><i>Book Reviews</i></b> .....		
<i>Contents of the June issue of Journal de Physique I</i> .....		953

Classification

*Physics Abstracts*

87.20 — 42.30 — 06.30

## Imaging optical thicknesses and separation distances of phospholipid vesicles at solid surfaces

Joachim Rädler and Erich Sackmann

Physik Department, Biophysics Group, Technische Universität München, James Franck Str. 1, 8046 Garching, Germany

(Received 16 October 1992, accepted in final form 18 January 1993)

**Abstract.** — We present the application of reflection interference contrast microscopy (RICM) (1) to map the optical density of supported bilayers and vesicles and (2) to image the contact profile of phospholipid vesicles at surfaces. The resolution in the surface profile is 0.2 μm laterally and 1 nm out of plane. The optical thickness of the membrane can be determined with 0.2 nm accuracy. We outline the theoretical basis of RICM and derive the interference intensities of adhering vesicles from first principles. An analytical expression for the decaying contrast of the interference fringes is given. The contact contour of vesicles is determined for various substrates. We further demonstrate that deposition of a magnesium fluoride layer on the glass substrate enhances the contrast and allows the optical density of adsorbed membranes to be imaged. By contrast variation of the buffer solution, the layer thicknesses and the indices of refraction can be measured. The novel method was applied to image lipid domains of different chain lengths in a substrate supported monolayer.

### Introduction.

Reflection interference contrast microscopy (RICM) is widely used in cell science to investigate cell adhesion. However, so far the technique has not been recognized to be a quantitative technique to determine optical thicknesses and separation distances of thin films. In his pioneering work Curtis [1] introduced RICM as a tool for cell scientists to investigate cell substrate interaction. The method was greatly improved by the invention of reflection contrast by Ploem in 1975 [2]. Considerable effort has been made to analyze RICM images in a quantitative manner to yield information about cell-substrate separation distances, membrane thicknesses and structures. Gingell, Todd and Heavens [3, 4] developed a method for numerical analysis of RICM considering the finite illumination aperture that resulted in a finite aperture interferometry theory. Due to the complexity of the cell structure, a quantitative analysis of RICM cell images is still disputed and limitations must be made in the interpretation of the cell substrate separation distance. An extensive review of these problems is provided by Verschueren [5].

To our knowledge, however, no systematic study of model membranes by RICM has been made to investigate the capability and limitations of RICM. We report the first experiments

using RICM to study giant phospholipid vesicles and supported lipid monolayers that allow a rigorous quantitative interpretation. The method was found to exhibit high accuracy in determining layer thickness and contact contours of membranes. The image formation of RICM can be cast into explicit analytic expressions of the interference intensity. We have treated the finite aperture effect analytically and present expressions for the decaying contrast and phase shift of the fringe pattern that are in good agreement with experimental results. The interference pattern of a spherical phospholipid vesicle adhering to the substrate can be derived from first principles and yield the membrane thickness as well as the contour and the separation distance of the vesicle.

It is further shown that deposition of  $MgF_2$  on the glass surfaces allows the investigation of membrane- and protein adsorption. A  $\lambda/8$  layer of  $MgF_2$  enhances the dependence of the reflected intensity on the thickness of the adsorption layer to 0.25 nm resolution. On the other hand RICM yields a high lateral optical resolution of 0.2  $\mu m$ . We demonstrate that in a supported monolayer at the glass-air interface the thickness difference of domains of phospholipids can be detected.

The intention of this article is to demonstrate that RICM has an excellent potential for the study of various structural and dynamical features of model membranes. The technique provides an imaging interferometric tool with ellipsometric thickness resolution and microscopic lateral resolution. It can be applied in combination with fluorescence and phase contrast microscopy. It is especially applicable for dynamical studies, as was demonstrated by a recent study of the surface undulation of red blood cells [6] and out of plane Brownian motion of latex beads [7].

The paper is divided into a theoretical and experimental section. In the first section we outline the basic principles of the reflection interference contrast microscopy. The crucial influence of the illumination and observation aperture of this technique is derived. Finally a new method of contrast enhancement by deposition of dielectric coatings is described. In the experimental section we describe a contrast variation experiment to determine the refractive index and thickness of lecithin bilayers and present first results on the investigation of giant vesicles interacting with an underlying substrate. Furthermore, examples of imaging microscopically heterogeneous film thicknesses are given.

## 1. Theory of RICM image formation.

**1.1 REFLECTION INTERFERENCE.** — The basic principle of reflection interference is depicted in figure 1. A sample is observed under monochromatic epi-illumination. The incoming beam with intensity  $I_0$  is partly reflected at the glass/water interface. We call the reflected beam reference beam  $I_1$ . The transmitted part is reflected from the object with an intensity  $I_2$ . The two beams interfere when imaged by the microscope objective onto the image plane. The observed total intensity  $I$  is described by the superposition of  $I_1$  and  $I_2$

$$I(\vartheta) = I_1 + I_2 + 2\sqrt{I_1 I_2} \cos [2kh(x)\cos\vartheta + \delta]. \quad (1)$$

The argument of the cosine contains the difference in the optical path length of the two beams. Here  $h(x)$  denotes the vertical object-substrate displacement as a function of the lateral position  $x$  and  $k$  denotes the wave vector  $k = 2\pi n/\lambda$  with  $n$  being the index of refraction of the medium. The constant phase  $\delta$  takes into account that the beam  $I_2$  might suffer an additional phase shift  $\delta = \pi$  at the medium-object interface if the object has a higher refractive index than the medium. The intensities  $I_1$  and  $I_2$  are related to the reflection coefficients of the interfaces by

$$I_1 = r_{01}^2 I_0 \quad I_2 = (1 - r_{01}^2)^2 r_{12}^2 I_0 \quad (2)$$

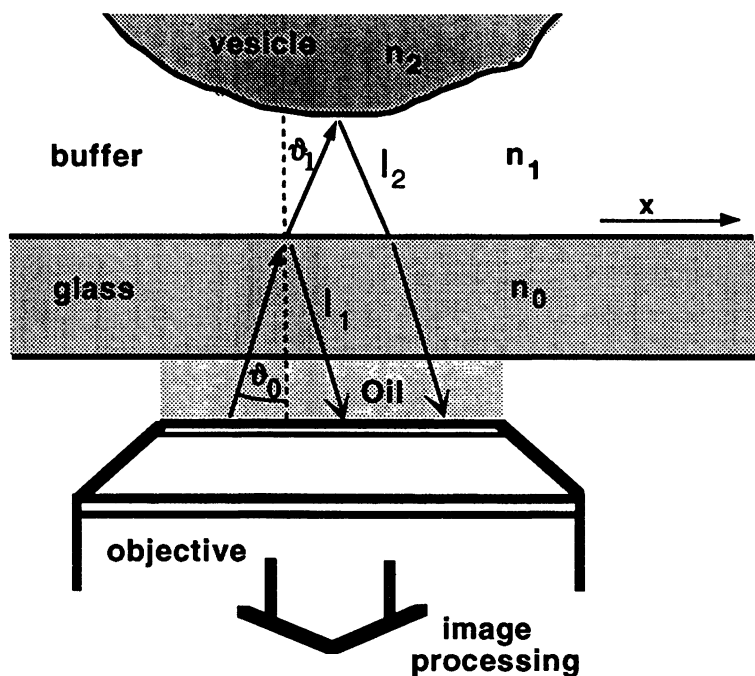


Fig. 1. — The basic principle of RICM: the object is observed under epi-illumination using monochromatic light. Interference fringes emerge from the difference in the optical path of light reflected from the object surface  $I_2$  and from the glass/buffer interface  $I_1$ .

where the amplitude reflection coefficients  $r_{ij}$  are given by the Fresnel equations

$$r_{ij}^s = \frac{n_0 \cos \vartheta_0 - n_1 \cos \vartheta_1}{n_0 \cos \vartheta_0 + n_1 \cos \vartheta_1} \quad r_{ij}^p = \frac{n_1 \cos \vartheta_0 - n_0 \cos \vartheta_1}{n_1 \cos \vartheta_0 + n_0 \cos \vartheta_1} \quad (3)$$

for s and p polarization with respect to the reflecting surface. The essence of equation (1) is that the observed image is a cosine transform of the object-substrate distance  $h(x)$  and therefore a transform of the lower side surface profile of the object. In this respect, RICM yields a holographic picture of the surface profile of microscopic objects. The three-dimensional reconstruction of the surfaces can be carried out by image processing. However, as we show below only surfaces close to the substrate can be investigated.

**1.2 REFLECTION CONTRAST.** — The intensity of the reflected monochromatic light is very low ( $10^{-3} I_0$ ) and consequently the observation of fringe pattern is usually obscured by stray light. This problem is overcome by the reflection contrast, also often called antiflex technique, that sufficiently reduces stray light [2]. The principle of the reflection contrast is illustrated in figure 2. A polarizer  $P_1$  produces linear polarized light in the illumination pathway. The light becomes circular polarized after passing the microscope objective that is covered with a  $\lambda/4$  plate at the top. The light reflected from the object passes the  $\lambda/4$  plate a second time and becomes linear polarized again, but is turned by  $90^\circ$  with respect to the illuminating beam. Therefore the object beam can pass the crossed analyzer  $P_A$  placed in the observation path, while stray light reflected from interfaces below the  $\lambda/4$  plate will not.

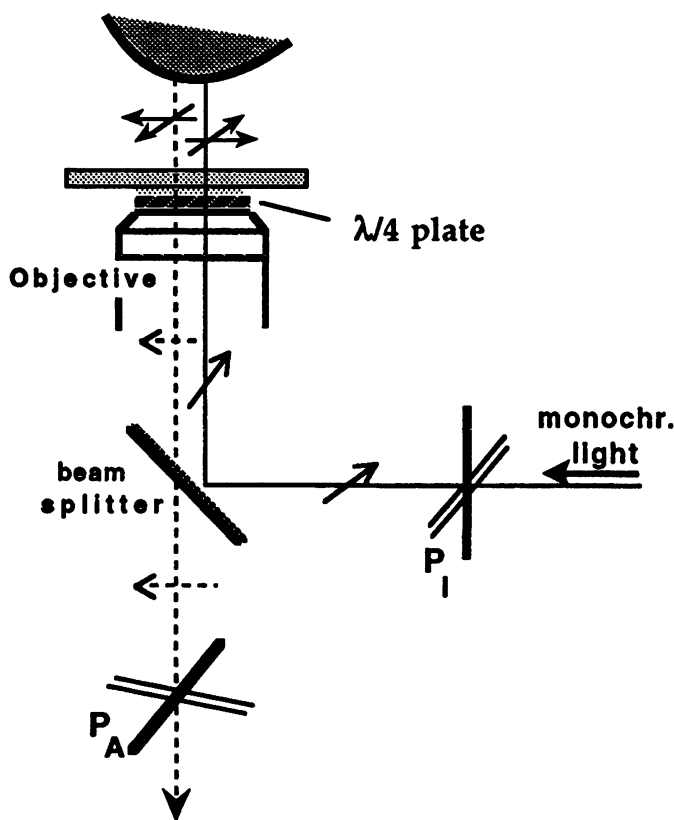


Fig. 2. — The contrast in reflection interference microscopy is enhanced by suppressing stray light with the antiflex technique. Light passing the Polarizer  $P_I$  and the  $\lambda/4$  plate on top of the objective becomes circular polarized. The reflected light becomes again linear polarized with the polarization turned by 90°. Therefore only the light reflected from the object passes the crossed analyzer  $P_A$  while stray light arising from intermediate lenses does not.

**1.3 FINITE ILLUMINATION APERTURE EFFECT.** — While in holographic microscopy coherent illumination is required, RICM uses monochromatic but incoherent illumination focused with high apertures. This leads to a rapidly decaying visibility of the higher order fringes. The effect has been numerically calculated by Gingell *et al.* [3, 4]. Their finite aperture theory simulates the aperture effect by incoherent summation of  $I(\vartheta)$  over all angles of illumination.

Applying equations (1-3) the integration can be written as follows

$$I = \int_0^{2\pi} \int_0^\pi w(\vartheta) |r_{01}(\vartheta) + (1 - r_{01}^2(\vartheta)) r_{12}(\vartheta) e^{i(2kh(x)\cos\vartheta + \delta)}|^2 \sin\vartheta d\vartheta d\varphi \quad (4)$$

where  $w(\vartheta)$  denotes the distribution function of the illuminating light with respect to the angle of incidence  $\vartheta$ . For the discussion of the numerical solution of this integral we refer to the work of Gingell *et al.* [3]. However, with the following approximations an analytical solution can be achieved. Firstly the intensity distribution function  $w(\vartheta)$  is approximated by a rectangular profile function for small apertures

$$w(\vartheta) = \begin{cases} I_0 & \vartheta \leq \alpha \\ 0 & \vartheta > \alpha \end{cases} \quad (5)$$

where  $\alpha = \vartheta_{\max}$  denotes the maximum illumination angle in the medium of refractive index  $n_1$ , which is related to the numerical illumination aperture INA by  $\alpha = \sin^{-1}[\text{INA}/n_1]$ .

Secondly, the angular dependence of the reflection coefficients  $r_{ij}$  is neglected. The later approximation is justified as follows. An expansion of the Fresnel equations (3) in powers of  $\vartheta$  yields to second order the approximation :

$$r_{ij}^{s, p} = \frac{n_i - n_j}{n_i + n_j} \left( 1 \pm \frac{n_i}{n_j} \vartheta^2 + O(\vartheta^4) \right). \quad (6)$$

Equation (6) shows that the reflectivity  $r_s$  increases with second order in  $\vartheta$  and  $r_p$  decreases. Since the antiflex technique, as described above, requires circular polarized light the integration has to be carried out over  $1/2(I_s(\vartheta) + I_p(\vartheta))$  to account for equal intensity of s and p polarization. Applying the expansion of equation (6) and collecting all terms in powers of  $\vartheta$  one finds that all the quadratic terms in  $\vartheta$  cancel. Therefore, the reflectivity of circular polarized light has an apparent weak dependence on the angle of incidence. Assuming constant reflectivity coefficients  $r_{ij}(\theta) \approx r_{ij}(0)$  the integration of equation (4) can be carried out

$$I = 2 \pi I_0 \int_0^\alpha |r_{01} + (1 - r_{01}^2) r_{12} e^{i(2kh \cos \vartheta + \delta)}|^2 \sin \vartheta d\vartheta \quad (7)$$

which results in

$$I = 4 \pi \sin^2 \alpha/2 \left[ I_1 + I_2 + 2 \sqrt{I_1 I_2} \frac{\sin(2kh \sin^2 \alpha/2)}{2kh \sin^2 \alpha/2} \cos [2kh(1 - \sin^2 \alpha/2) + \delta] \right] \quad (8)$$

where  $I_1$  and  $I_2$  are defined in equation (2). Equation (8) shows two important features of the finite aperture effect. The contrast or the visibility  $\nu$  of the interference fringes usually defined as

$$\nu = \frac{I_{\max} - I_{\min}}{I_{\max} + I_{\min}} \quad (9)$$

decays with increasing distance and aperture like  $\sin(y)/y$ .

$$\nu = \frac{2 \sqrt{I_1 I_2} \sin(y)}{I_1 + I_2}, \quad y = 2kh \sin^2 \alpha/2. \quad (10)$$

Secondly, the phase is stretched by a factor of  $1 - \sin^2 \alpha$ . Both results are in agreement with experimental observations. In figure 3 we show the fringes of a water wedge between two glass plates for two different illumination apertures. It is clearly seen that the decay of the experimental fringe amplitudes follows equation (8). The fitted lines in figures 3a and 3b differ in only one parameter, which is the aperture angle  $\alpha$ . There is however one curious phenomenon in figure 3b. The function  $\sin(y)/y$  becomes negative for a certain range of  $y$ . Hence a sudden phase shift  $\pi$  is expected, when  $\sin(y)/y$  equals zero. This phenomenon is known as contrast reversal. However the data seem to avoid an obvious jump in phase and exhibit a significant deviation from equation (8) in this critical region.

**1.4 WAVE-OPTICAL DESCRIPTION OF THE FINITE ILLUMINATION APERTURE EFFECT.** — The theoretical result described above can also be derived in a wave optical picture from the classical theory of coherence. Let us assume a quasi-monochromatic and incoherent light source and consider the situation depicted in figure 4a. Two pinholes in the object plane O are

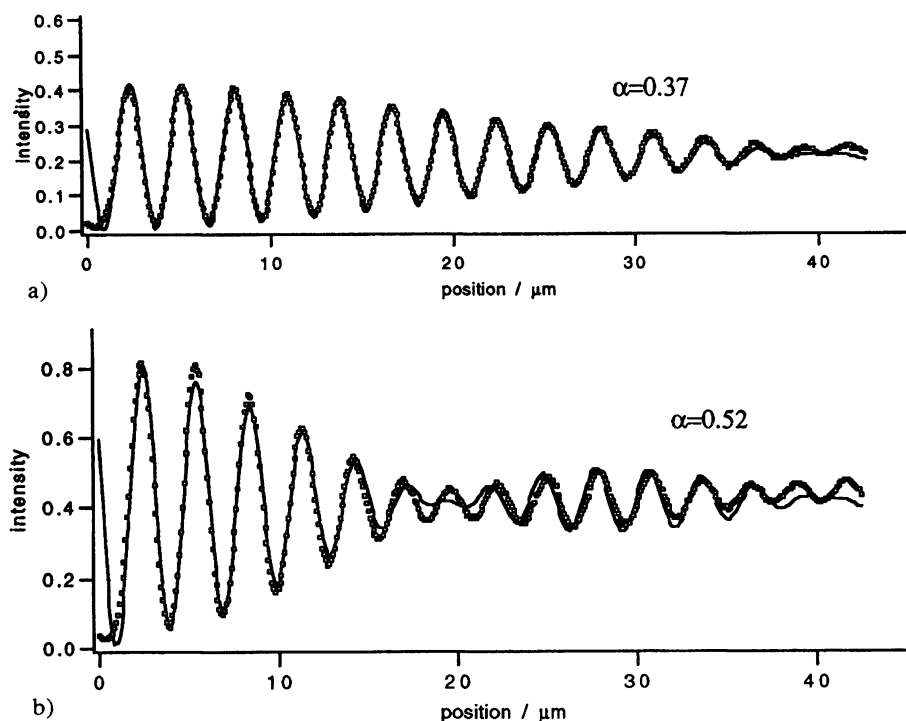


Fig. 3. — Interference pattern of a water wedge between two glass plates measured for two different apertures. The full lines represent the theoretical expression for the finite illumination aperture effect given by equation (8). The theoretical functions in a) and b) differ in only one parameter, the maximum illumination angle  $\alpha$ .

illuminated by the incoherent light through the lens L with aperture A. The out coming beams  $I_1$  and  $I_2$  interfere in the image plane S. Since the illumination is assumed to be perfectly incoherent there will be no interference visible unless the pinholes are very closely adjacent. The light then becomes partial coherent and the degree of interference is described by the mutual coherence function  $\Gamma_{12}$  defined through

$$I = I_1 + I_2 + 2 \sqrt{I_1 I_2} \Gamma_{12} \cos [2 kh(x) + \delta] \quad (11)$$

$\Gamma_{12} = 0$  corresponds to total incoherence, while  $\Gamma_{12} = 1$  equals the fully coherent case. According to the Van Citter-Zernike theorem the mutual coherence function is equal to the Fourier transform of the intensity distribution of the incoherent source in the aperture plane A, which again is given by the amplitude spread function of the illumination optics [8].

The situation in reflection interference corresponds exactly to the situation described above. It is shown in figure 4b that the light reflected from the glass/buffer interface can be regarded as pinhole 1 and the light reflected from the object as coming from a virtual pinhole 2 at a distance  $2 h(x)$ . The mutual coherence  $\Gamma_{12}$  is again given by the amplitude spread function. But in this case the amplitude spread function has to be taken along the axis out of focus. The three-dimensional intensity of the Airy pattern near the focus was calculated by Debye [8]. The amplitude spread function  $u_p$  is given by

$$u_p = \Gamma_{12} = \frac{\sin(y)}{y} e^{iy}, \quad y = 2 kh \sin^2 \alpha/2. \quad (12)$$

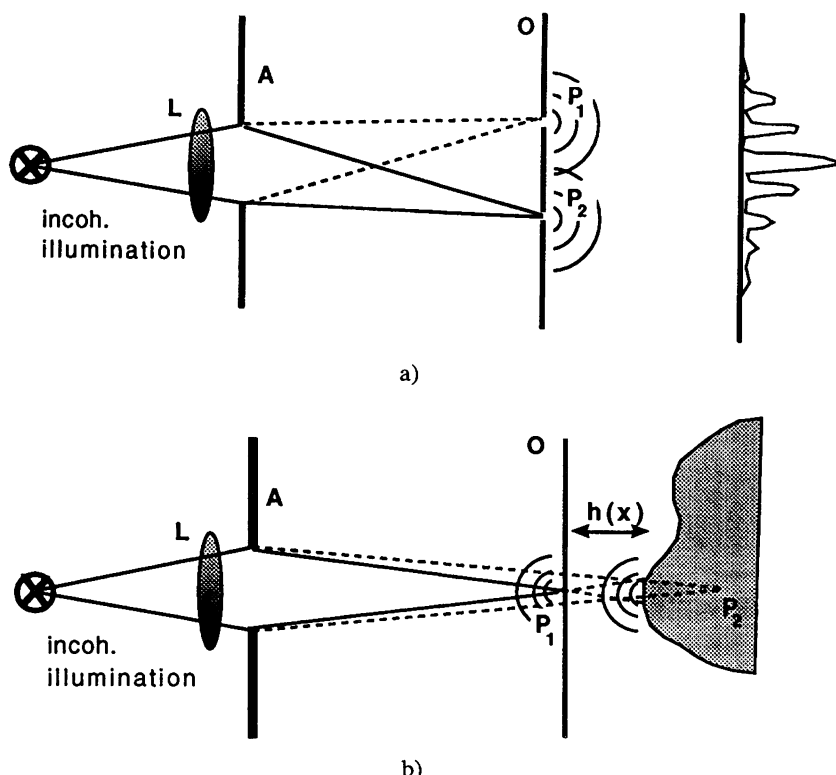


Fig. 4. — Wave optical description of the finite illumination aperture effect. a) Light emitted from two pinholes  $P_1$  and  $P_2$  becomes partial coherent, if the distance of the pinholes is comparable to the half width of the Airy pattern of the incoherent illumination. b) Correspondingly in RICM light reflected from the glass interface and reflected from the object is partial coherent for small  $h(x)$ . If the object is removed from the object plane  $O$  the coherence and therefore the interference pattern is eventually lost.

Substituting this expression into equation (11) yields directly the previous result of equation (8). The above calculation shows that the finite aperture effect can be considered as a problem of partial coherence between the two reflecting interfaces. The reflected light loses coherence as the object moves out of focus of the illumination.

**1.5 SPATIAL RESOLUTION.** — Most objects of interest that are investigated by RICM will exhibit curved surfaces in contact with a flat substrate. This also implies that the fringes narrow as the gradient,  $\partial h / \partial x$ , of the contour at the edge increases. For small objects and steep gradients the fringe pattern will consequently reach the limit of spatial resolution of the microscope. In other words, fringes of high lateral spatial frequency will be additionally damped beside the effect caused by the finite illumination aperture described above. The total damping is readily described by the normalized optical transfer function  $\tau(k_x)$

$$\tilde{I}_{\text{img}}(k_x) = \tilde{I}_{\text{obj}}(k_x) \cdot \tau(k_x) \quad (13)$$

where  $I_{\text{obj}}(k_x)$  denotes the object spectrum and  $I_{\text{img}}(k_x)$  the image spectrum as a function of the spatial frequency variable  $k_x$ . The spatial frequency  $k_x$  is determined by the slope of the contour

$h(x)$  according to

$$k_x = 2 k \partial h / \partial x . \quad (14)$$

Following the optical transfer function of our imaging system has to be determined. It turns out that the optical transfer function of a microscope becomes rather complicated in the case of partial coherent illumination and exhibits non linearity. However, for the following discussion it will be sufficient to consider the so-called apparent transfer function of the fundamental spatial frequency component. An explicit expression has been calculated by Becherer and Parrent [9]

$$\tau(k_x) = \begin{cases} 1 & 0 < k_x < b - a \\ 3 \frac{b + a - k_x}{b + 5a - k_x} & b - a < k_x < b + a \\ 0 & b + a < k_x \end{cases} \quad (15)$$

with  $a = 2 \pi n / \lambda \cdot \text{INA}$  and  $b = 2 \pi n / \lambda \cdot \text{NA}$  where INA denotes the numerical illumination aperture and NA the numerical aperture of the objective. The transfer function varies as a function of the ratio  $b/a$  between a step function for  $b/a \rightarrow \infty$  (coherent case) and a linearly decaying function for  $b/a \rightarrow 0$  (incoherent case). We are now able to explicitly include the spatial resolution in equation (8). The observed intensity becomes finally

$$I = I_1 + I_2 + 2 \sqrt{I_1 I_2} \Gamma_{12}(h)_\alpha \tau(k_x)_\alpha, \beta \cos [\Phi(h)_\alpha] \quad (16)$$

here  $\phi(h)$  describes in short the phase of the interference as above  $\phi(h) = 2kh(1 - \sin^2 \alpha/2) + \delta$  and the indices  $\alpha$  and  $\beta$  indicate dependence on the illumination and observation aperture respectively.

We conclude that contours with gradients steeper than a limiting slope exhibit interference pattern damped by the optical resolution of the microscope. The limiting slope is given by  $\partial h / \partial x|_{\max} = n/n_{\text{glass}} (\text{NA} - \text{INA})$  as derived from equations (14) and (15). We obtain  $34^\circ$  degrees as the limiting slope for  $\text{INA} = 0.48$  and  $\text{NA} = 1.25$ . For gradients larger than  $57^\circ$  the fringes will eventually vanish, since the optical transfer function equals zero.

RICM can also be used to image different optical densities rather than contours. In this case the lateral resolution of heterogeneity in a planar layer can also be derived from the optical transfer function equation (15). Applying the classical Rayleigh criterion the resolution is about  $0.2 \mu\text{m}$  for an objective with  $\text{NA} = 1.25$ .

**1.6 IMAGING MEMBRANES AND MULTILAYERS.** — So far we have analyzed the interference of two reflecting interfaces to explain the principles of RICM. Yet in general the object as well as the substrate might be composed of layers with many interfaces. We will reduce the latter case to the case of two interfaces by calculating the effective complex reflection amplitudes for both the layered object and the substrate and insert these into equation (8) as derived above.

Let us consider the reflected light from a single membrane of thickness  $d$ . The membrane has two surfaces and the complex reflection coefficient is given by Drudes Formula [10].

$$R = r_{WM} \frac{1 + e^{2kd}}{1 + r_{WM}^2 e^{2kd}} \quad (17)$$

where  $r_{WM}$  denotes the Fresnel coefficient of the water/membrane interface. The interference function of the membrane at a distance  $h(x)$  above a substrate can be calculated by equation (8)

replacing  $I_2 = |R|^2 I_0$  and  $\delta = \arctan(\text{Im}(R)/\text{Re}(R))$ . This theoretical function is shown in figure 5 (full line). Note that multiple reflectance between the membrane and the substrate is neglected in this case.

There are two noteworthy properties in the interference function (Fig. 5). Both arise from the fact that a membrane is very thin and the reflected light of the two interfaces interferes almost entirely destructive due to the phase difference of  $\pi$ .

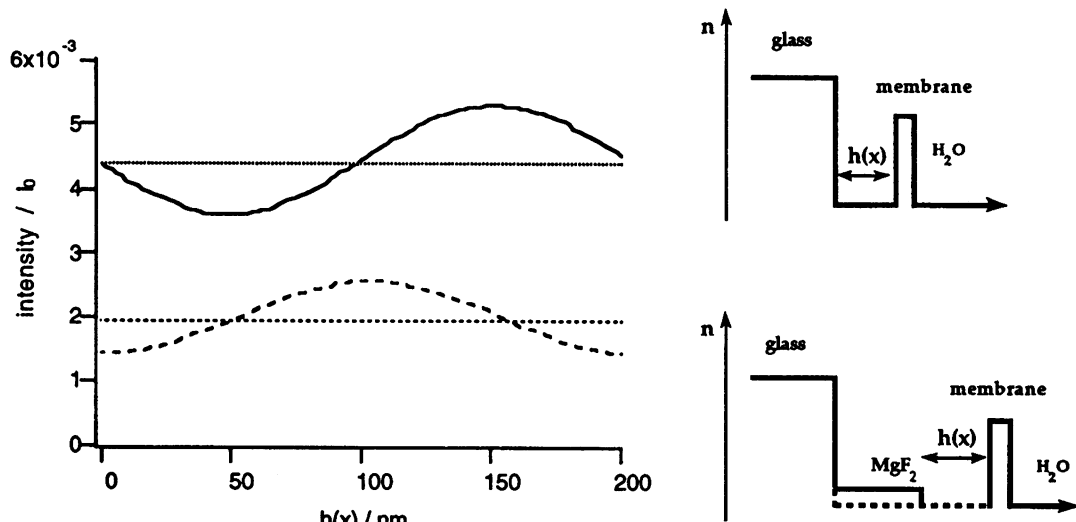


Fig. 5.— Theoretical interference intensity normalized with respect to  $I_0$  of a phospholipid membrane as a function of the membrane-substrate (glass) distance  $h(x)$ . The amplitude of the oscillating intensity is proportional to the thickness of the membrane (here 43 Å). An  $\text{MgF}_2$  antireflection coating of 60 nm deposited on the glass surfaces shifts the phase of the interference [dashed line] and enhances the contrast between the interference and the background intensity.

Firstly, for small membrane thicknesses the intensity difference  $I_{\max} - I_{\min}$  is proportional to the membrane thickness  $d$ . This can be seen by approximating  $I_2$  from equation (17).

$$I_2 = R^2 I_0 \approx 4 r_{\text{MW}}^2 \sin^2(kd) I_0. \quad (18)$$

Applying equation (1) we obtain an expression for the contrast of the interference fringes

$$\frac{I_{\max} - I_{\min}}{I_1} = \frac{8 r_{\text{MW}}}{r_{\text{GIW}}} \sin(kd) \quad (19)$$

$I_{\max}$ ,  $I_{\min}$  and  $I_1$  can be measured from the maximum, the minimum and the background intensity of the membrane interference pattern. Therefore equation (19) provides a tool for measuring the membrane thickness with great precision, since the difference in intensities divided by the background intensity is not sensitive to fluctuations of the incoming light  $I_0$ , which are the major impairment for quantitative measurements. We discuss the resulting membrane thicknesses in the experimental section.

Secondly, the effective phase of the light reflected from a membrane is approximately  $\delta \approx \pi/2 + 2kd$ . This implies that the intensity as a function of the membrane-substrate distance varies sinusoidal rather than following a cosine function. A membrane in contact with

the glass surface yields an intensity that is nearly indistinguishable from the background intensity. Therefore adsorbed films and membranes are hardly visible at a pure glass interface. As will be shown below, the situation is different if a dielectric layer is deposited on the glass surface.

**1.7 CONTRAST ENHANCEMENT BY MgF<sub>2</sub> DEPOSITION.** — The optical effect of a dielectric coating on the interference function is also shown in figure 5. A layer of 60 nm magnesium fluoride (MgF<sub>2</sub>) decreases the background intensity and at the same time shifts the interference phase such, that a membrane in contact with the substrate is clearly distinguishable from the background. The dielectric layer can be considered as a spacer adjusting the reflectivity of the glass/buffer interface to the reflectivity of the membrane as well as shifting the phase of the interference. Note that thereby the contrast as defined in equation (9) increases by a factor of 1.5.

Let us now consider the sensitivity in optical density detection achieved by the deposition of MgF<sub>2</sub>. Let the thickness of the dielectric layer be  $L$ . After adsorption of an arbitrary layer of thickness  $\Delta d$  onto the dielectric the intensity changes by  $\Delta I$ . Neglecting multiple reflection the relative change in intensity is given by :

$$\frac{\Delta I}{I} \Big|_{d=0} = \frac{2 r_{12} r_{23} \sin 2 kL}{r_{01}^2 + r_{13}^2 + 2 r_{01} r_{13} \cos 2 kL} 2 k \Delta d \quad (20)$$

where the indices 0, 1, 2, 3 indicate glass, MgF<sub>2</sub>, adsorband, buffer. Equation (20) states that maximum sensitivity is achieved for a  $\lambda/8$  coating, if the denominator is only weakly varying ( $r_{01} \gg r_{13}$ ). We obtain a thickness resolution for adsorbed layers of  $\Delta d \approx 0.25$  nm at the MgF<sub>2</sub>/air interface and  $\Delta d \approx 0.5$  nm at the MgF<sub>2</sub>/water interface assuming an intensity resolution of 1 % and a MgF<sub>2</sub> coating thickness of  $L = 50$  nm.

Beside the fact that adsorbed membranes become visible, the deposition of a MgF<sub>2</sub> layer solves a more general problem in RICM that is the unique reconstruction of a surface or height profile. As can be seen from figure 5 the interference intensity of a membrane does not relate uniquely to a membrane-substrate separation distance. For investigations of membranes close to a substrate it is an advantage that the intensity relates uniquely to the separation distance in the range of 0 to 100 nm as in the case of a MgF<sub>2</sub>-coated surface. In this regime the reconstruction of the contour is independent of additional topological assumptions and can be carried out by a direct mapping of the intensity field onto a height profile. This is especially important for dynamical investigations of contour fluctuations close to the surface.

## 2. Experimental section.

**2.1 MICROSCOPE SETUP.** — A Zeiss Axiomat microscope was modified for reflection interference contrast observation as follows. Epi-illumination was provided by a 100 W high pressure mercury lamp. A heat absorption filter and a bandpass filter ( $d\nu = 5$  nm, 85 % peak transmission) was used to select the green 546.1 nm Hg line. The illumination numerical aperture was adjustable and was measured by the illumination cone in a 1 cm thick glass block. The smallest value available for the INA was 0.48. The microscope was equipped with a Zeiss Neofluar 63/1.25 Antiflex objective. For proper working of the antiflex contrast enhancement two polarizers were situated in the illumination and observation pathway respectively, as described above. Fluorescence microscopy could be performed by switching to a dichroic mirror — barrier filter set. Phase contrast microscopy could be used simultaneously with RICM by using additionally dia-illumination and placing a phase ring in the Fourier plane. The RIC images were recorded by a CCD camera (HR480, Aqua TV, Germany) at a rate of 25

frames per second. A frame comprised  $604 \times 588$  pixels. The magnification of the image could be varied by a set of intermediate optical lenses. Image processing was carried out on a Datacube image processing system (Datacube Peabody, Boston, USA). The images were digitized into 256 gray levels. For static image analysis the data were averaged over 8 frames to reduce camera noise. To account for the nonlinearities of the camera, an intensity gauge curve was recorded by placing a set of six different transmission filters in the optical path. The gauge curve was fitted by a polynomial function and the measured intensities corrected accordingly.

**2.2 SAMPLE PREPARATION.** — Synthetic lecithins were purchased from Avanti Polar Lipids (Birmingham, AL). Within this article we use the conventional short notation as denoted in brackets : L- $\alpha$ -dimyristoyl-1,2-diacyl-sn-glycero-3-phosphocholine (DMPC), L- $\alpha$ -dipalmitoyl-1,2-diacyl-sn-glycero-3-phosphocholine (DPPC) and 1-stearoyl-2-oleoyl-sn-glycero-3-phosphocholine (SOPC).

Giant vesicles consisting of DMPC, DPPC and SOPC were prepared as follows. Lipid was dissolved in a stock solution of 10 mg/ml chloroform/methanol (2 : 1). 40 ml of the solution was dried on a teflon disk and desiccated under vacuum for 2 hours. Subsequently 100 mM sucrose solution was added to the teflon disk placed at the bottom of the glass beaker and left for 24 hours at 40 °C. The lipid swells on top of the teflon and forms closed vesicles. Some ml of the vesicle suspension was transferred into a measuring chamber filled with 100 mM inositol solution. The vesicles sediment slowly to the bottom of the chamber due to the difference in density of sucrose inside the vesicle and inositol outside. The measuring chamber was made out of a teflon frame (20 × 20 × 4 mm) embedded in a temperature controlled copper block. The teflon frame was closed at the bottom by a coverslip and positioned on the microscope stage. The refractive indices of the buffer solutions were measured independently with an Abbe refractometer.

Thin films of magnesium fluoride on glass coverslips were prepared by vacuum deposition. The glass was previously cleaned in 2 % Hellmanex solution. MgF<sub>2</sub> deposition took place at a pressure of  $10^{-6}$  atm with a deposition rate of about 1 nm/s at a substrate temperature of 380 °C. The film thickness was measured by a quartz thickness monitor. The layer thickness was also cross-checked by the transmission spectrum of the sample using an absorption spectrometer.

**2.3 MEASUREMENT OF THE REFRACTIVE INDICES AND MEMBRANE THICKNESSES BY CONTRAST VARIATION.** — Lecithin vesicles strongly adsorb onto freshly deposited magnesium fluoride. Most vesicles rupture when touching the MgF<sub>2</sub> surface and spread out to a single flat bilayer patch. The membrane is seen as a dark patch in RICM due to the interference effect described in section 1.7. An example is shown in figure 6a. The rupture and spreading of the vesicles takes place within milliseconds. In this article, however, we want to focus on the optical properties of an adsorbed membrane. With RICM we measure one gray level associated with the optical thickness of a patch of lecithin. To measure both the index of refraction and the absolute thickness of the adsorbed bilayer patch, a classical contrast experiment can be carried out by varying the refractive index of the aqueous buffer by adding glycerol. Within the same sample we observed the intensity at different positions on the uncoated (glass/buffer) and the coated interface (glass/MgF<sub>2</sub>/buffer and glass/MgF<sub>2</sub>/lipid(buffer)). Figure 6b shows the reflected intensities as a function of the refractive index of the glycerol/water solution. The intensities are normalized to the percentage of light reflected at the glass/water interface. The fitted lines are calculated by using the appropriate expression for the reflectivity of stratified layers taking multiple reflection into account [10]. The first graph yields the refractive index of glass, the second and third successively the refractive index and layer thickness of the magnesium

fluoride and the lipid bilayer. We measured in several experiments patches of DMPC, DPPC and SOPC. The averaged refractive index found for  $MgF_2$  ( $1.386 \pm 0.002$ ) is in very good agreement with published data. For the averaged refractive index of the lecithins a value of  $1.49 \pm 0.01$  was specified which is in good agreement with the value measured by Chapman *et al.* [11]. Fitting the intensities for the different lipid patches with the constant averaged value of the refractive index for lecithins, we obtain different lipid bilayer thicknesses as listed in figure 6. Published data on lecithin membrane thicknesses vary to some extend depending on

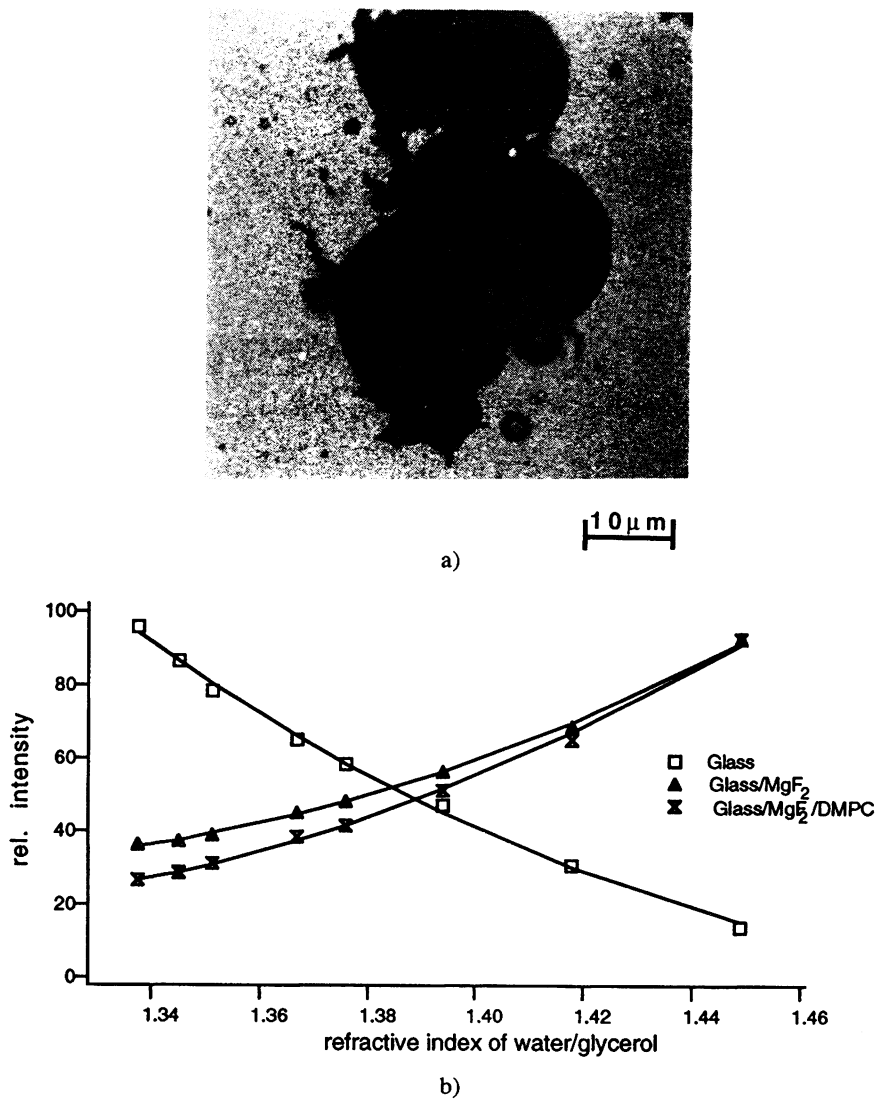
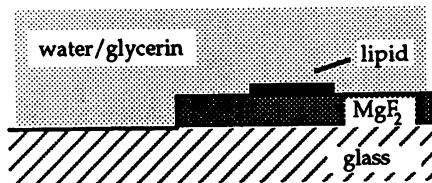


Fig. 6. — a) RICM micrograph of a lecithin (DMPC) vesicle that is ruptured and spread out to a flat a patch of supported bilayer on  $MgF_2$ . b) Contrast variation experiment : the refractive index of the buffer is changed by addition of glycerol. The intensities at three spots of different interface composition is measured. The indices of refraction and the layer thicknesses are obtained from the fit to the theoretical reflectivity of stratified layers. The intensities are normalized with respect to the reflectivity of the glass/water interface.



$$\begin{aligned}
 n_{\text{glass}} &= 1.532 \pm 0.004 \\
 n_{\text{MgF}_2} &= 1.386 \pm 0.002 \\
 n_{\text{lipid}} &= 1.486 \pm 0.01 \\
 d_{\text{MgF}_2} &= 69.9 \pm 0.3 \text{ nm}
 \end{aligned}$$

$$\begin{aligned}
 d_{\text{DMPC}} &= 3.4 \pm 0.6 \text{ nm} \\
 d_{\text{DPPC}} &= 4.7 \pm 0.5 \text{ nm} \\
 d_{\text{SOPC}} &= 4.0 \pm 0.5 \text{ nm}
 \end{aligned}$$

c)

Fig. 6. — c) Indices of refraction and layer thicknesses as obtained from figure 6b.

the experimental method [11-13]. Our results agree best with X-ray scattering data [13]. The experimental error in our optical method does not allow a detailed comparison between the different scattering techniques. The thickness of the adsorbed layer may be determined with an accuracy of about 0.5 nm in a contrast variation experiment. The membrane thicknesses are determined more precisely from the interference fringes of giant vesicles as described in the next chapter. However, we are able to distinguish the relative thickness increase of the bilayer with increasing length of the fatty acid chains. It should also be noted that at the observation temperature of 30 °C the DMPC bilayer is in the fluid ( $L_\alpha$ ) phase, while the DPPC bilayer is in the solid ( $L_\beta$ ) phase. This explains the large difference in the bilayer thicknesses of DMPC and DPPC, since the  $L_\beta$  phase is known to be thicker than the  $L_\alpha$  phase. For the same reason the thickness of DPPC was found to be larger than that of SOPC which is in the  $L_\alpha$  phase due to the unsaturated chain.

**2.4 VESICLE MEMBRANE THICKNESS, CONTACT SHAPES AND SEPARATION DISTANCE.** — We applied RICM to study the shape of phospholipid vesicles adhering to different substrates. In this chapter we interpret four examples of RICM micrographs of vesicles that are given in figures 7-10. Each figure contains a photographic presentation of the RICM image, an intensity plot, a schematic drawing of the vesicle shape and finally the experimentally determined contour function. The evaluation of the contour is based on equation (8) of section 1.3. We describe the contour function  $h(x)$  in terms of several parameters and determine these parameters by fitting the analytic interference function (Eq. (8)) to the experimental fringe pattern. A different approach is demonstrated in the last example. There we directly relate intensity values to separation distances in a regime where a unique mapping is possible.

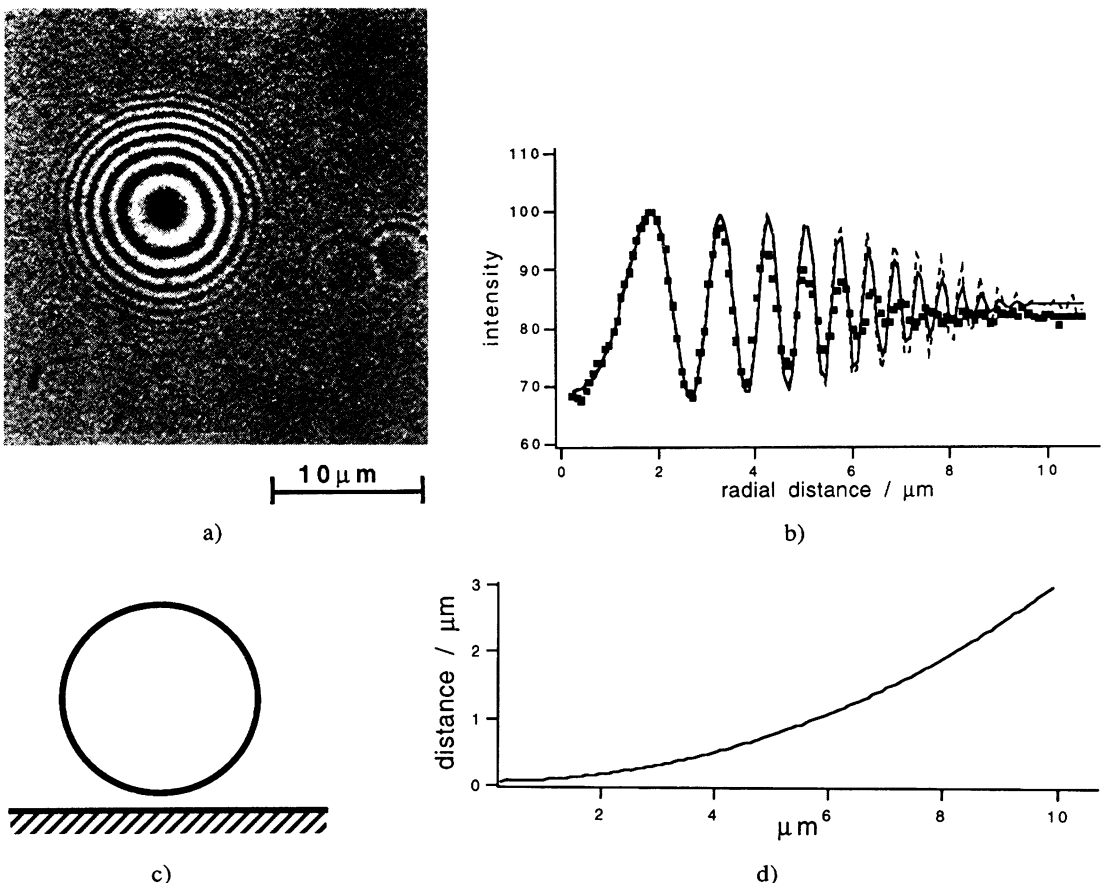


Fig. 7. — a) RICM image of a spherical giant phospholipid (DMPC) vesicle with radius 16  $\mu\text{m}$ . c) Schematic view of spherical vesicle close to the substrate. b) (■) Angularly averaged intensity plot of figure 7a. The dashed curve indicates the theoretical interference function of a sphere obtained by equation (8), the fully drawn curve includes the finite spatial resolution effect according to equation (16). The discrepancy between the curves for the higher order fringes is explained in the text. d) Calculated spherical contour corresponding to the fit in b).

Firstly we studied the RIC pattern of a spherical vesicle, in which case the contour is given by

$$h(x) = h_0 + R - \sqrt{R^2 - x^2}. \quad (21)$$

Figure 7a depicts the corresponding RICM image, which exhibits the well known Newtonian rings. The shape is perfectly spherical, since the vesicle is under weak osmotic pressure. The vesicle is filled with 100 mM sucrose inside and floats in a 100 mM inositol solution above a pure glass surface. The gravitational force determined by the slight difference in density of the sugar solutions and the van der Waals force push the vesicle towards the substrate. On the other side the electrostatic force, due to the high surface potential of glass and some impurity charges on the vesicle, prevents the vesicle from touching the glass surface [7]. The angularly averaged intensity of the pattern in figure 7a is plotted in figure 7b. The data points are compared with

the theoretical intensity function given by equation (8) (dashed) and by equation (16) (full line) that additionally includes the optical transfer function.

The experiment shows that as the gradient of the contour increases the fringes are more strongly damped as predicted. In fact neither the effect of the finite illumination aperture nor of the finite optical resolution fully describes the decay of the fringes. The discrepancy can be understood as an effect due to the curvature of the vesicle surface. For parallel surfaces equation (8) predicts an intensity  $I_1 + I_2$  in the limit where coherence between the two interfaces is lost. The experimental intensity, however, approaches the background intensity  $I_2$  for large radial distances, as expected, since the vesicle has a finite diameter. The difference between the theoretical and the experimental curve shown in figure 7b equals in fact  $I_1$ . Therefore the theoretical description of the damping of the fringes of strongly curved surfaces remains unsatisfactory. However, the interference intensity of the quasi flat part of the vesicle that is closest to the substrate is well described by the theoretical function derived in section 1.

The spherical contour assumed in the fit is confirmed by the data. Note that the information on the shape of the object is comprised only in the phase of the interference pattern and not affected by the damping due to curvature and finite aperture effects. The fit yields the same vesicle radius as determined in phase contrast microscopy.

As described in the above discussion of equation (19) in section 1.7 the thickness of the membrane can be obtained from the difference  $I_{\max} - I_{\min}$  of the first fringes. Here we obtain  $3.8 \pm 0.2$  nm for the membrane thickness of the DMPC vesicle. This value is reasonable for a single bilayer and within the standard deviation of the thickness obtained for the adsorbed DMPC membrane in 2.3.

We now consider vesicles adhering to the substrate. Two cases are studied : strong and weak adhesion. Adhesion of vesicles to surfaces has been studied experimentally and theoretically [14-16]. In the case of strong adhesion the vesicle takes the shape of a spherical cap. In the contact region, however, the membrane is bent smoothly rather than forming a sharp contact angle with the underlying substrate. On the other hand weakly bound vesicles may display a variety of shapes determined by the bending stiffness and exhibiting thermally excited surface undulations.

We induced adhesion of DMPC vesicles to a glass surface by adding  $\text{CaCl}_2$  to the sugar buffer. Figure 8a presents an example of a multilamellar vesicle adhering to glass in a buffer containing 90 mM inositol and 10 mM  $\text{CaCl}_2$ .

We expect the vesicle to be flat in the adhering part and quasi-spherical otherwise. We therefore fitted the interference function of a sphere to the higher order fringes of the data (dashed curve). There is good agreement in the phase from the first fringe on. As expected the fit yields a negative sphere substrate distance and the data do not fit the intensities for the adhering middle region.

We describe the contact contour of the adhering middle region by the following polynomial function

$$h(x) = \begin{cases} h_0 & \text{for } x < x_0 \\ h_0 + a(x - x_0) + b(x - x_0)^2 + c(x - x_0)^4 & \text{else .} \end{cases} \quad (22)$$

The contour is flat in the adhering part ( $x < x_0$ ) and deviates for  $x > x_0$ . The fit is represented by the full line in figure 8b. The coefficients were  $x_0 = 2.2 \mu\text{m}$ ,  $a = 0.0001$ ,  $b = 0.04$  and  $c = 0.001$ . Therefore the vesicle shape near the contact zone is clearly second and forth order. As figure 8d shows, the fitted contour functions (full line and dashed) smoothly merge into each other.

The good contrast of the image figure 8a indicates already a multilamellar membrane. In

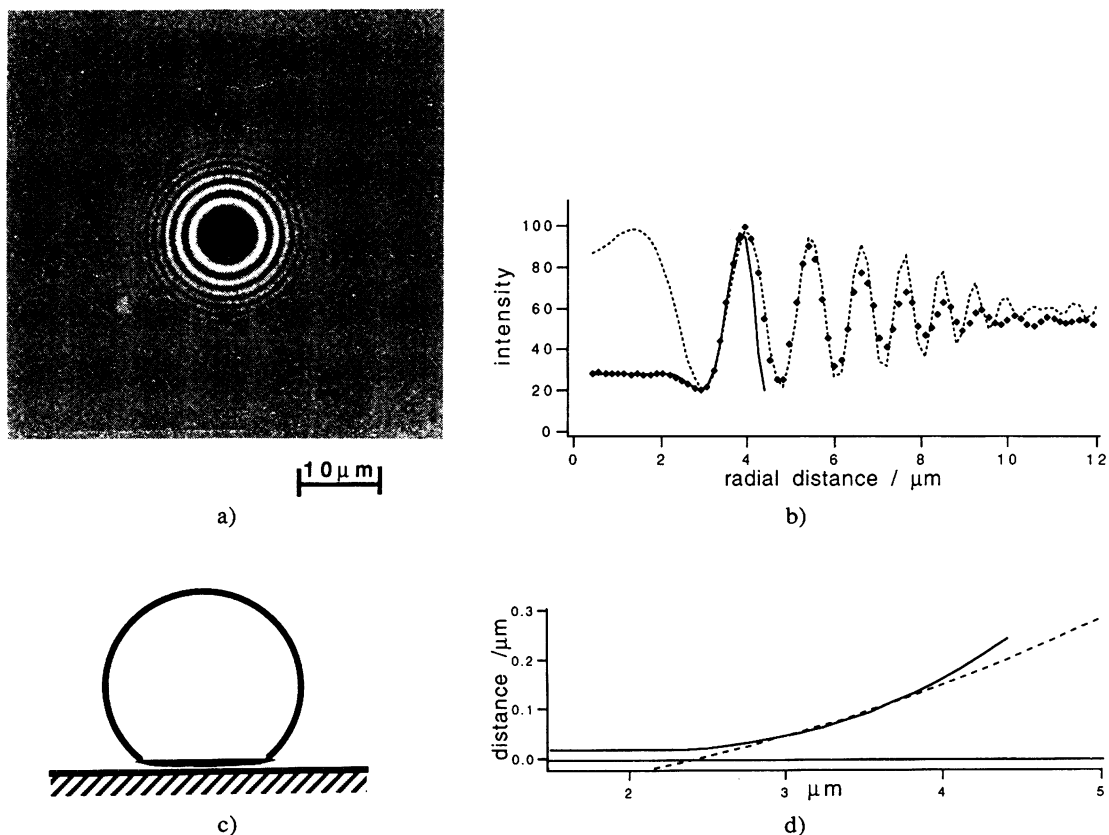


Fig. 8. — a) RICM micrograph of multilamellar vesicle adhering on glass in 10 mM CaCl<sub>2</sub> 100 mM inositol buffer. b) Dependence of the angularly averaged intensity as a function of the radial distance from the center of the vesicle. The vesicle is flat in the adhering center part and exhibits a parabolic contact contour (full line). The higher order fringes fit to a quasi-spherical shape (dashed line). c) Schematic view of adhering vesicle. d) Calculated contour functions (parabolic and quasispherical) in the contact region corresponding to the fitted interference functions in b).

fact the measured intensity difference  $I_{\max} - I_{\min}$  corresponds to the intensity expected for a model membrane composed out of 4 bilayers of 3.75 nm thickness separated each other by 2.7 nm.

The ratio of area to volume of a vesicle can be changed by changing the osmolarity of the buffer solution. Deflating a vesicle that strongly adheres to a surface, leads to a flat bound shape as depicted schematically in figure 9c. In contrast to the last example the interference will arise from the upper part of the vesicle in this case. The lower part of the vesicle is plainly stretched out and does not contribute to the observed pattern with the exception of a constant phase shift. The edges of the contour are strongly curved, while the upper part builds a flat spherical cap. Figure 9a shows as such an example a DPPC vesicle adhering to a pure MgF<sub>2</sub> surface. Since the boundary of the adhering part is not completely circular, we dispense with the angular average and present in figure 9b a sectional scan along the vertical axis through the center of the vesicle. The data are fitted with the interference function of a sphere. Obviously the sphere is a good approximation at least in the middle part. The contrast yields 4.4 nm ± 0.2 nm for the DPPC membrane thickness.

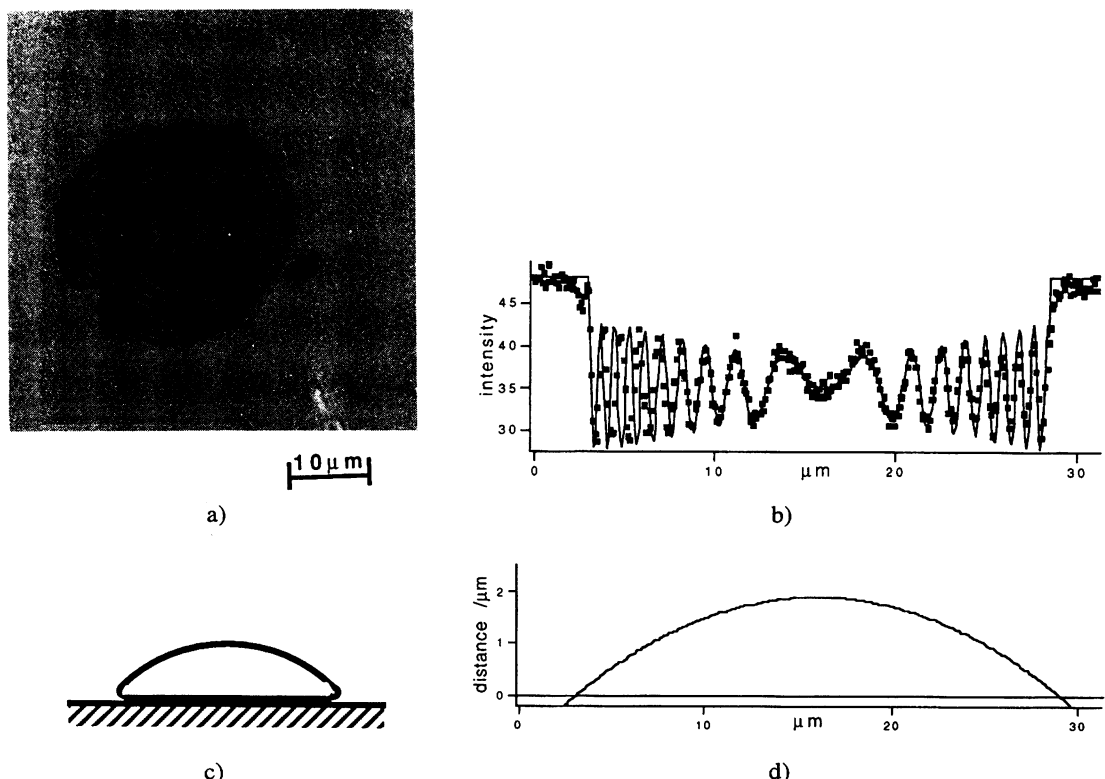


Fig. 9. — a) RICM micrograph of a DPPC vesicle strongly adhering on a  $\text{MgF}_2$  surface. b) The intensity profile along a vertical axis through the center of the vesicle. The full line depicts the interference curve of a spherical cap above the adhering flat part. c) Schematic view of strongly adhering flat vesicle. d) Calculated contour corresponding to the fit in b).

It is important to note that in general the interference pattern of any closed object will be a superposition of the light reflected from the upper and lower part of the object. For flat objects that do not fully adhere, the interpretation of fringes becomes considerably more complicated. Therefore the last two examples are special cases in which the contour can be clearly defined. Of course equation (16) enables to estimate the contribution of the reflectance of the upper membrane that will be damped with increasing thickness of the object.

The last example in figure 10 presents a weakly bound vesicle. In this case pronounced thermal undulations of the membrane are visible which, in the former examples, were suppressed by lateral tension induced by osmotic pressure or by strong adhesion [15]. To measure the fluctuating separation distance of the membrane directly we followed the phase shift technique described in section 1.7.

Firstly 56 nm  $\text{MgF}_2$  was deposited on glass. Then the  $\text{MgF}_2$  surface was covered with a DMPC bilayer by fusion of strongly sonicated vesicles. The probe was carefully rinsed buffer to remove small residual vesicles. Eventually a vesicle suspension of giant SOPC vesicles was added. The buffer contained 20 mM NaCl and 100 mM inositol. The vesicles were filled with 100 mM sucrose. Under these conditions the vesicles adhere only weakly to the  $\text{MgF}_2$ -bound bilayer and thermal undulations are excited. The undulations are clearly visible as transient, dynamic displacements of the fringes. In the adhering part the intensities fluctuate about an average gray value but never reach the maximal possible intensity of the first fringe of the non-

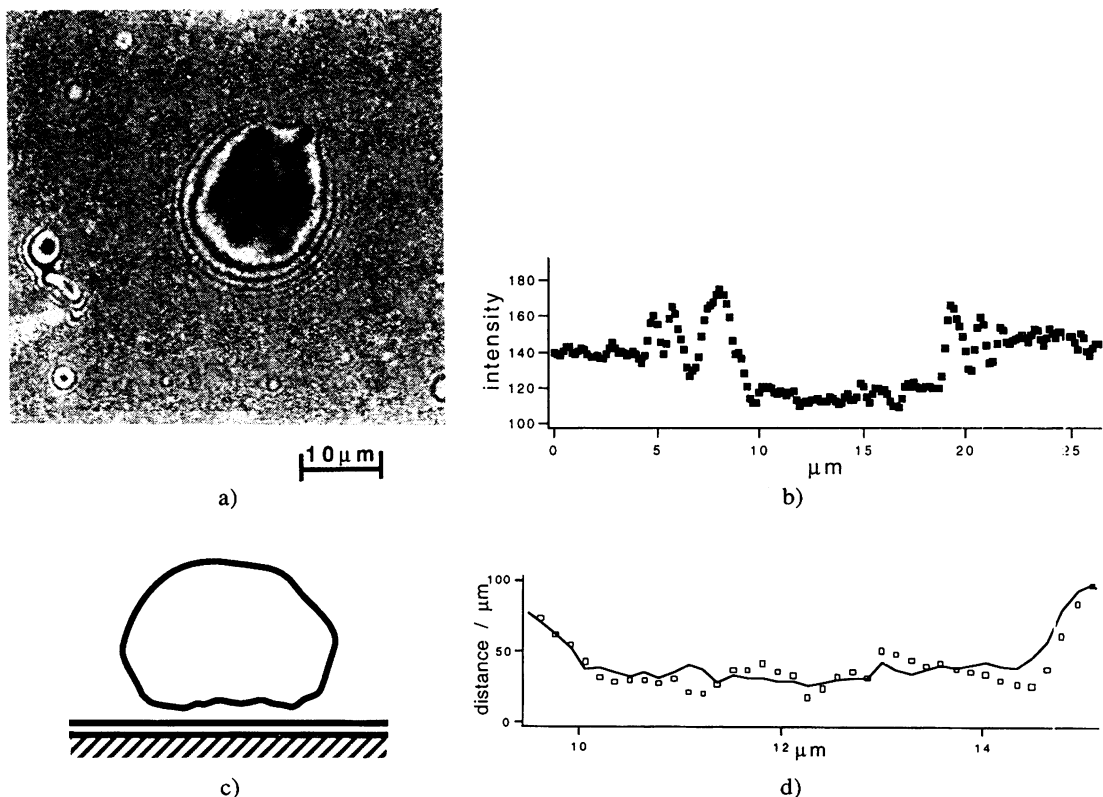


Fig. 10. — a) RICM micrograph of a weakly adhering SOPC vesicle on a DMPC covered  $MgF_2$  surface. The fringes are distorted due to strong thermal fluctuations. b) An intensity profile along the horizontal axes through the center of the vesicle. c) Schematic view of weakly bound vesicle exhibiting undulations. d) Surface profile calculated directly from the intensities in the adhering region (between 8 and 18  $\mu m$ ). (□) : momentaneous profile, full line : surface profile averaged over 16 frames.

adhering part. Figure 10b shows a snapshot of the intensity profile along the horizontal axis of the vesicle. The intensities are related to the separation distance as depicted already graphically in figure 5a. As long as the variation in the distance is smaller than 100 nm we can directly map the intensity to a height profile. Figure 10d shows a snapshot of the height profile (dots) and also an average over 16 frames (full line). The time averaged mean square amplitude in the flat part is  $110 \text{ nm}^2$ .

This type of experiment allows the momentaneous height profile of a membrane bound by a weak potential for each video frame to be determined. From the data the full time-space correlation function of the undulations can be obtained by image processing [6]. We will publish the dynamic evaluation of the vesicle adhesion experiments elsewhere.

**2.5 SUPPORTED MONOLAYERS AT THE GLASS-AIR INTERFACE.** — In the last chapter we demonstrate the application of RICM for adsorption and structural investigations such as lateral phase separation in monolayer and anisotropic textures in the different liquid crystalline phases of membranes.

Figure 11 shows the example of protein adsorption onto  $MgF_2$  covered glass. The reflected intensity was observed as a function of BSA-concentration added to the bulk. From this the thickness of adsorbed BSA shown in figure 11 was determined. The thickness of the

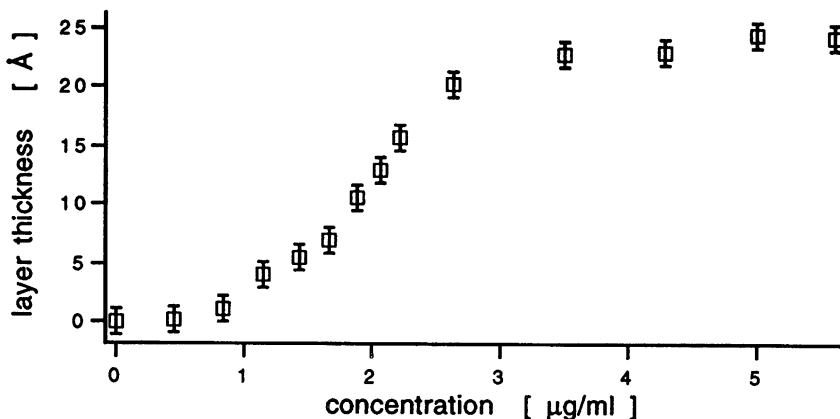


Fig. 11. — Adsorption isotherm of bovine serum albumin (BSA) onto  $\text{MgF}_2$  measured by RICM. The thickness is calculated according to equation (20) from the decreases in intensity due to the adsorbed layer. The refractive index of BSA is assumed to be 1.55.

$\text{MgF}_2$  layer was chosen to be 50 nm to achieve high sensitivity according to equation (20). BSA was found to adsorb much stronger to  $\text{MgF}_2$  than, for example, to silicon oxide. Furthermore no adsorption was observed in a separate experiment for polylysine (MW3800) onto  $\text{MgF}_2$ . Both facts strongly indicate a positive surface charge of  $\text{MgF}_2$ .

Figure 12 shows an observation of lateral phase separation in lipid mixtures. A monolayer of a 1 : 1 mixture of L- $\alpha$ -dilauroyl-1,2-diacyl-sn-glycero-3-phosphocholine (DLaPC (12 CH<sub>2</sub>

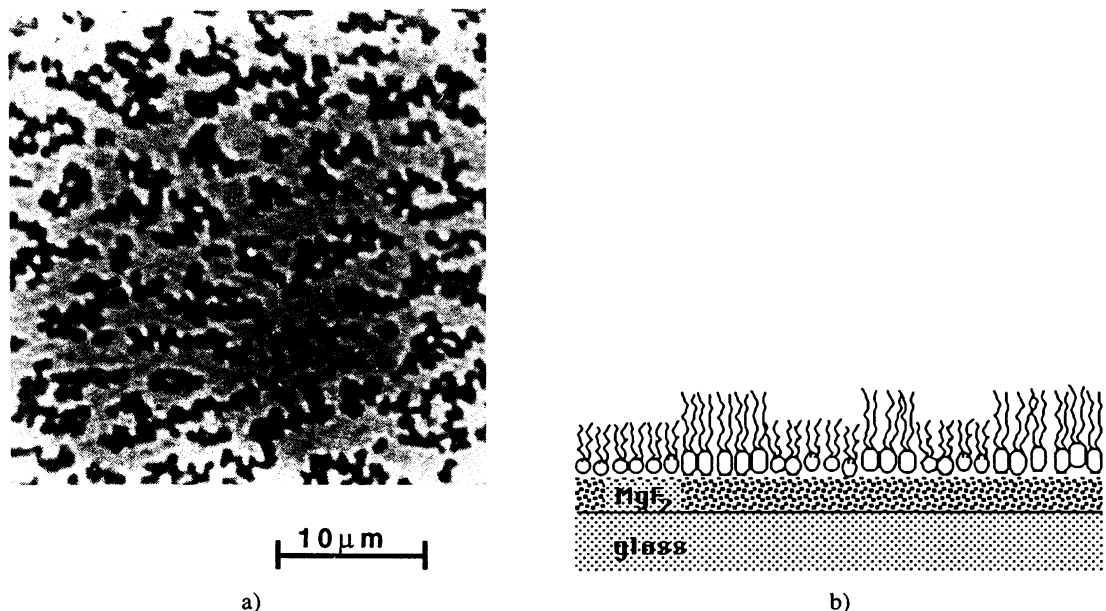


Fig. 12. — a) RICM image of a supported monolayer exhibiting lateral phase separation on  $\text{MgF}_2$ . The film is a 1:1 mixture of DLaPC and DLiPC transferred from the film balance. b) Schematic view of a phase separated supported lipid monolayer.

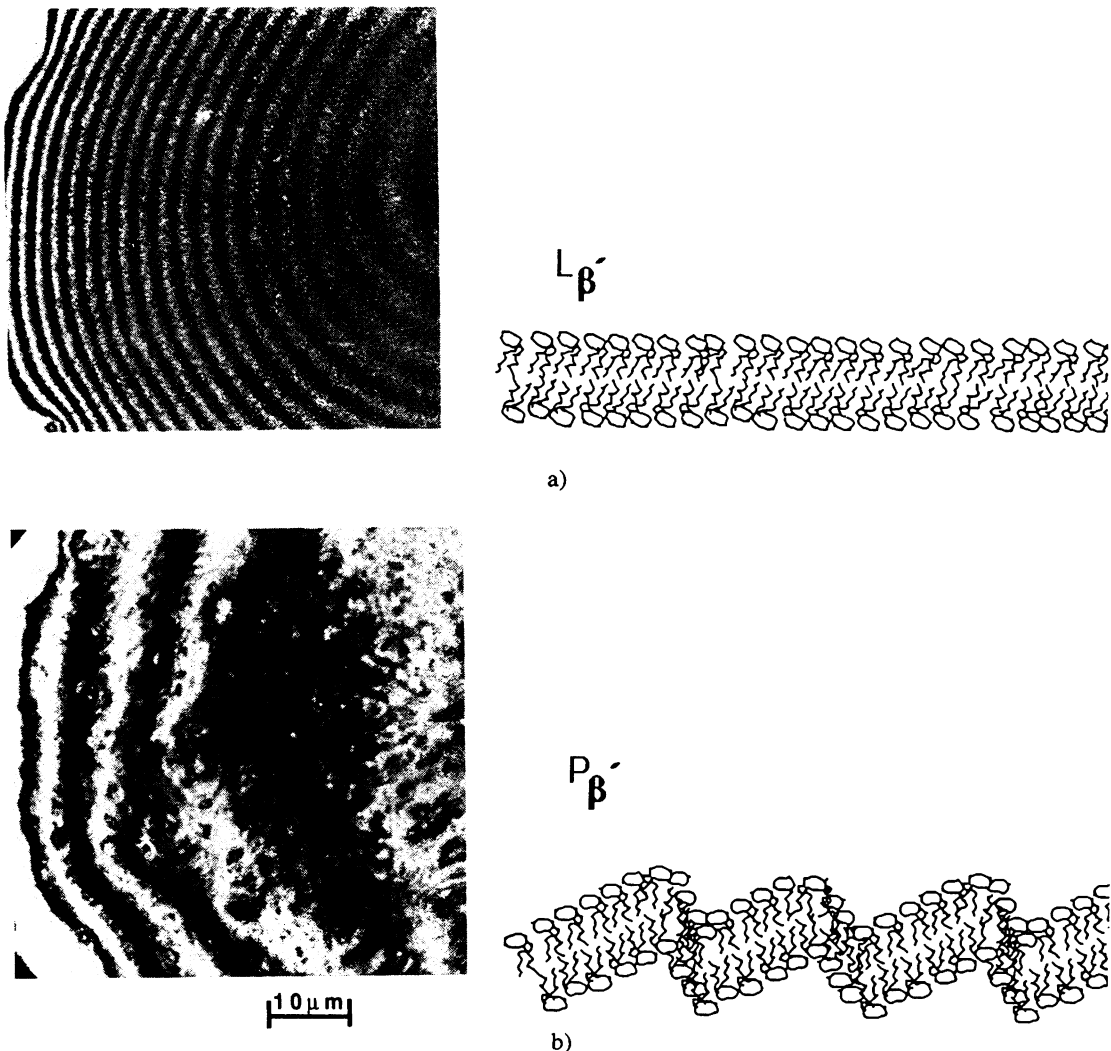


Fig. 13. — a) DPPC vesicle (at 38 °C) under tension due to strong adhesion of the surface. Vesicle is in the  $L_{\beta'}$  phase since the corrugated  $P_{\beta'}$ -gel-state (the ripple phase) is suppressed by the tension. b) The same vesicle after further cooling leading to leakage and loss of volume and tension. The membrane undulates weakly and exhibits a texture associated with the  $P_{\beta'}$  phase.

groups per chain) and L- $\alpha$ -dilignoceroyl-1,2-diacyl-sn-glycero-3-phosphocholine DLiPC (24 CH<sub>2</sub> groups per chain) was spread on a film balance. At room temperature phase separation occurs leading to a laterally inhomogeneous layer with small circular domains rich in DLiPC. The existence of such domains on the film balance was observed with fluorescence microscopy. The film was then transferred onto a MgF<sub>2</sub> covered glass cover slip at a pressure of 32 mN/m. Figure 12 depicts the RICM micrograph of the monolayer after deposition. As clearly seen in figure 12 the domains become visible in RICM. The dark regions are composed of small circular domains that had clustered during the film transfer. The appearance of the domains on MgF<sub>2</sub> is in perfect agreement with the corresponding fluorescence micrograph of the transferred film.

Bilayers of synthetic lecithins exhibit different phases due to their long-range organization in the bilayer. The most common are the liquid-like ( $L_\alpha$ ), the corrugated gel-phase ( $P_{\beta'}$ ) (ripple phase) and the homogeneously tilted gel-phase ( $L_\beta'$ ). As a last application we studied the optical surface roughness of vesicles in the two gel phases. Figure 13a shows the RICM image of a DPPC vesicle in the  $L_\beta'$  and figure 13b in the  $P_{\beta'}$  phase. The  $L_\beta'$  appears smooth in contrast to the  $P_{\beta'}$  phase that exhibits a characteristic texture. The vesicle strongly adheres to a  $MgF_2$  surface similar to the one in figure 9. In the beginning the temperature is about 38 °C and the vesicle is under stress. In this case the  $L_\beta$  phase is preferred, while the ripple phase is suppressed. Figure 13b presents the same vesicle after having lost volume due to leakage in the process of further cooling. A surface roughness clearly appears. It is attributed to the surface texture of the  $P_{\beta'}$  phase which is formed after relaxation of the lateral stress. As is well known from freeze fracture electron microscopy the  $P_{\beta'}$  ripple phase exhibits a polygonal surface profile due to orientational defects of the Néel-waal type [17]. The arrangement of stripes visible in figure 13b are interpreted as domains of opposite orientation of the ripples separated by Néel waals. However a quantitative interpretation of the phenomenon can not yet be given.

### Discussion.

We have reformulated the theoretical basis of RICM and developed a method for quantitative measurements of the refractive indices and thicknesses of membranes by RICM. Moreover, the thicknesses of the membranes of adhering giant vesicles may be determined from the contrast of the first fringes with an accuracy of 0.2 nm. The values are in agreement with published data. Therefore RICM may be applied in future to determine the thickness of more complex systems like polymer or protein coated vesicles. We have furthermore demonstrated that RICM allows surface profiles of objects close to the underlying substrate to be reconstructed. Equilibrium shapes, contact angles and especially contact curvatures can be measured. The measurements of surface curvature will yield information on adhesion forces relative to bending stiffness [14-16]. The high lateral and time resolution makes RICM an ideal technique to study the elastic properties, flickering phenomena and phase changes of model membranes at surfaces. In particular lateral phase separation in giant vesicles can be detected without the aid of fluorescent labels.

A unique feature of RICM is that it allows the membrane thickness of vesicles in aqueous suspension close to a surface to be determined. It is thus distinguished from laterally resolving ellipsometry [18] or Brewster angle microscopy [19, 20], which are designed to image the optical density variation in a lipid monolayer at the air-water or air-solid interface.

A possible drawback of RICM might be that it is bound to transparent substrates, which usually means glass or coated glass. RICM can, however, also be applied on mica, if mica is cut very thin and deposited optically matched on a supporting glass cover slip. We obtained undistorted images of adhering vesicles on mica that can be at least interpreted in a qualitative manner. Furthermore various crystals might prove suitable as a substrate for RICM studies.

### Acknowledgments.

The work was supported by the Deutsche Forschungsgemeinschaft through the Sonderforschungsbereich SFB 266. Further support by the Fond der Chemischen Industrie is gratefully acknowledged. One of us (J. R.) likes to thank E. Evans for stimulating discussions and hospitality at the UBC, Vancouver.

## References

- [1] CURTIS A. S. G., The mechanism of adhesion of cells to glass. A study by interference reflection microscopy, *J. Cell Biol.* **20** (1964) 199.
- [2] PLOEM J. S., Reflection-contrast microscopy as a tool for investigation of the attachment of living cells to a glass surface. Appeared in : Mononuclear Phagocytes in Immunity, Infection and Pathology, R. V. Furth Ed. (Oxford, Blackwell Scientific Publications, 1975).
- [3] GINGELL D. and TODD I., Interference Reflection Microscopy. A Quantitative Theory for Image Interpretation and its Application to Cell-Substratum Separation Measurements, *Biophys. J.* **26** (1979) 507.
- [4] GINGELL D., TODD I. and HEAVENS O. S., Quantitative interference microscopy : effect of microscope aperture, *Opt. Acta* **29** (1982) 901.
- [5] VERSCHUEREN H., Interference Reflection Microscopy In Cell Biology : Methodology and Applications, *J. Cell Sci.* **75** (1985) 279.
- [6] ZILKER A., ENGELHARD H. and SACKMANN E., Dynamic reflection interference contrast (RIC-) microscopy : a new method to study surface excitations of cells and to measure membrane bending elastic moduli, *J. Phys. France* **48** (1987) 2139.
- [7] RÄDLER J. and SACKMANN E., On the Measurements of Weak Repulsive and Frictional Colloidal Forces by Reflection Interference Contrast Microscopy, *Langmuir* **8** (1992) 848.
- [8] BORN M. and WOLF E., Principles of Optics, 4th Ed. (Pergamon Press, 1970).
- [9] BECHERER R. J. and PARRENT G. B., Nonlinearity in Optical Imaging Systems, *J. Opt. Soc. Am.* **57** (1967) 1479.
- [10] AZZAM R. M. A. and BASHARA N. M., Ellipsometry and polarized light (North-Holland, Amsterdam, 1975).
- [11] CHERRY R. J. and CHAPMAN D., Optical Properties of Black Lecithin Films, *J. Mol. Biol.* **40** (1969) 19.
- [12] JOHNSON S. J., BAYERL T. M., McDERMOTT D. C., ADAM G. W., RENNIE A. R., THOMAS R. K. and SACKMANN E., Structure of an adsorbed dimyristoylphosphatidylcholine bilayer measured with specular reflection of neutrons, *Biophys. J.* **59** (1991) 289.
- [13] LIS L. J., MCALISTER M., FULLER N., RAND R. P. and PARSEGIAN V. A., Interaction between neutral phospholipid bilayer membranes, *Biophys. J.* **37** (1982) 657-665.
- [14] EVANS E. and PARSEGIAN V. A., Energetics of Membrane Deformation and Adhesion in Cell and Vesicle Aggregation, *Ann. N.Y. Acad. Sci.* (1983) 13.
- [15] SERVUSS R. M. and HELFRICH W., Mutual adhesion of lecithin membranes at ultralow tensions, *J. Phys. France* **50** (1989) 809.
- [16] SEIFERT U. and LIPOWSKY R., Adhesion of vesicles, *Phys. Rev. A* **42** (1990) 4768.
- [17] RÜPPEL D. and SACKMANN E., On defects in different phases of two-dimensional lipid bilayers, *J. Phys. France* **44** (1983) 1025.
- [18] ERMAN M. and THEETEN J. B., Spatially resolved ellipsometry, *J. Appl. Phys.* **60** (1986) 859.
- [19] HENON S. and MEUNIER J., Microscope at the Brewster angle : direct observation of first order phase transition in monolayers, *Ren. Sci. Instrum.* **62** (1991) 936-939.
- [20] HÖNIG D. and MÖBIUS D., Direct Visualization of Monolayers at the Air-Water Interface by Brewster Angle Microscopy, *J. Phys. Chem.* **95** (1991) 4590-4592.